

Journal of Materials Chemistry C

Materials for optical, magnetic and electronic devices

Accepted Manuscript

This article can be cited before page numbers have been issued, to do this please use: B. Kumela, R. Anvari and W. Wang, *J. Mater. Chem. C*, 2025, DOI: 10.1039/D5TC02423D.



This is an Accepted Manuscript, which has been through the Royal Society of Chemistry peer review process and has been accepted for publication.

Accepted Manuscripts are published online shortly after acceptance, before technical editing, formatting and proof reading. Using this free service, authors can make their results available to the community, in citable form, before we publish the edited article. We will replace this Accepted Manuscript with the edited and formatted Advance Article as soon as it is available.

You can find more information about Accepted Manuscripts in the [Information for Authors](#).

Please note that technical editing may introduce minor changes to the text and/or graphics, which may alter content. The journal's standard [Terms & Conditions](#) and the [Ethical guidelines](#) still apply. In no event shall the Royal Society of Chemistry be held responsible for any errors or omissions in this Accepted Manuscript or any consequences arising from the use of any information it contains.

Interfacial Electronic Structure Modulation by Facet Orientation and Sulfur Vacancies in CdS/MoS₂ Heterojunctions[†]

Beniam Kumela,^a Roozbeh Anvari,^a and Wennie Wang^{a‡}

We investigate how facet orientation and sulfur vacancies influence the interfacial charge transfer properties of CdS/MoS₂ heterojunctions. Using density functional theory, we find that the (001)-CdS/MoS₂ interface exhibits a Type-III band alignment, while the (100)-CdS/MoS₂ forms a homojunction-like alignment that straddles the water redox potentials, making it more suitable for overall water splitting. Furthermore, sulfur vacancies induce localized charge redistribution in the (100)-CdS/MoS₂ interface, with select configurations introducing shallow defect states that may aid in the charge transfer pathways of hydrogen evolution reactions through favorably aligned dipole moments. In contrast, sulfur vacancy configurations in the (001)-CdS/MoS₂ interface produce a more uniform charge redistribution and minimal changes to the electronic structure. The resulting dipole moments in the (001)-CdS/MoS₂ may instead limit desired interfacial charge transfer. Finally, we find that defect formation energy differences reveal a facet-dependent tendency to form sulfur vacancies in CdS/MoS₂.

1 Introduction

Continuously growing hydrogen demand has been predominantly met through non-renewable sources, underscoring the urgent need for sustainable production alternatives^{1–3}. Photocatalytic water splitting utilizes sunlight to drive hydrogen production, offering a green alternative that may circumvent the high costs associated with electrolysis systems, such as the reliance on rare earth catalysts⁴ and extensive electrical infrastructure requirements^{5,6}.

To improve the efficiency of photocatalysis, research is focused on materials that minimize charge carrier recombination⁷ and utilize the high irradiance, visible range of light (1.63–3.26 eV)⁸. Among several candidates, cadmium sulfide (CdS) shows great promise as its bulk crystal has a band gap of 2.42 eV⁹ and is comprised of earth abundant constituents. However, CdS photocatalytic performance is known to suffer from significant photocorrosion^{10,11} and recombination¹².

Several experiments have observed heterojunction photocatalysts as a path to resolve the shortcomings of CdS¹³. At a heterojunction interface, dissimilar energy alignment of the band edges results in charge carrier transport across the two materials. If the bands form a staggered (Type-II) alignment, this can result in charge carrier separation which reduces recombination and enhances photocatalytic efficiency. Zong et al. found that loading MoS₂ onto CdS yields the highest photocatalytic activity compared to loading with noble metals¹⁴. This is particularly interesting because platinum (Pt), one of the co-catalysts tested, is well known to outperform MoS₂ as a promoter for H₂ evolution in electrochemical systems, a trend explained by its position near the peak of the volcano plot relating exchange current den-

sity to free energy of adsorption of hydrogen¹⁵. Thus, the authors suggest the heterojunction formed between MoS₂ and CdS is important for enhancing the photocatalytic activity. Although a performance increase has been observed with MoS₂, the mechanism behind this enhancement remains unclear. Liu et al. reported an increase in incident photon-to-current efficiency (IPCE) and a reduction in photoluminescence (PL) for CdS loaded with MoS₂¹⁶. Based on Mott-Schottky (M-S) analysis, they proposed that the improved efficiency arises from reduced recombination, which is attributed to charge separation resulting from the formation of p–n heterojunctions. Min et al. observed that the increase CdS/MoS₂ photocatalytic activity is sustained after more than 4 hours of irradiation¹⁷. This led them to propose the formation of a Type-I band alignment facilitating hole transfer from CdS to MoS₂ and causing the MoS₂ to act as a sacrificial agent that inhibits CdS corrosion. Conversely, Ma et al. observed CdS corrosion in CdS/MoS₂ during stable H₂ production¹⁸. Using heterogeneous nucleation theory, they proposed that sulfur vacancies on MoS₂ serve as recrystallization sites for degraded CdS ions, corroborated by similar observations in CdS/WS₂¹⁹.

In parallel to experiments, several first-principles studies attempt to further elucidate the mechanisms behind the efficiency of CdS/MoS₂. Modeling the cubic-CdS/MoS₂ system using monolayers within the density functional theory (DFT) framework, Lian et al. found that the interface resembles a p–n heterojunction with a built-in potential of 0.45 eV, which could be responsible for observed electron-hole separation²⁰. Zhang et al. compared the (001) and (100)-CdS/MoS₂ heterostructures with a monolayer or bilayer of CdS to find that (100)-CdS/MoS₂ exhibits more favorable properties for photocatalytic performance, such as a stronger binding energy, expanded light absorption edge, and faster hole migration speed²¹. Using time-dependent density functional theory (TDDFT), Cheng et al. identified two sequential mechanisms—electron-phonon coupling and interfacial

^a McKetta Department of Chemical Engineering, The University of Texas at Austin, USA.

[‡] E-mail: wwwennie@che.utexas.edu.

[†] Supplementary Information available: [details of any supplementary information available should be included here]. See DOI: 00.0000/00000000.



dipole-driven state alignment—that govern charge separation in (001)-CdS/MoS₂, leading to gradual then rapid electron transfer across the interface²².

Although previous studies have highlighted several important mechanisms by which CdS/MoS₂ heterojunctions enhance its photocatalytic efficiency, several critical effects remain unaddressed or only partially considered. As previously noted, the exact nature of the heterojunction observed in experiments remains uncertain, with various studies reporting a homojunction¹⁶, Type-I^{23–25}, or Type-II^{26,27} band alignments. A possible explanation for these discrepancies lies in the fact that several studies have determined band alignment based on band edges of isolated CdS and monolayer MoS₂, prior to heterojunction formation. However, these band edges can shift upon heterojunction formation due to interfacial dipole moments and strain—though the direction and magnitude of this shift remain unexplored for the CdS/MoS₂ interface. To the best of our knowledge, no prior computational studies have modeled full slab representations of both experimentally relevant CdS facets—(001) and (100)²⁸—in contact with MoS₂.

The role of the interfacial defects in CdS/MoS₂ is also under explored. Vacancies and other intrinsic defects can enhance light absorption by introducing mid-gap states, which enable sub-bandgap photon excitation and broaden the absorption spectrum²⁹. These defect states have been proposed to improve charge separation by acting as temporary trapping sites for photo-generated carriers, thereby reducing the probability of direct electron–hole recombination³⁰. Sulfur vacancies in MoS₂ have been shown to activate the otherwise inert basal plane for hydrogen evolution reactions (HER) by tuning the free energy of adsorption of hydrogen closer to 0 at specific concentrations^{31,32}. This not only enhances catalytic activity but also improves charge utilization by facilitating electron transfer to adsorbed hydrogen intermediates. However, the role of defects at the interface has seen limited study. To address these gaps, we systematically investigate changes in band alignment at the CdS/MoS₂ heterojunction, the effects of interfacial dipole formation, and the impact of point defects on the electronic structure and charge redistribution. To do this, we use full slab models of experimentally relevant CdS facets interfaced with monolayer MoS₂ with and without sulfur vacancies. This approach will lead to a deeper understanding of the mechanisms that enhance photocatalytic efficiency in CdS/MoS₂.

This paper is organized as follows. In Sec. 2, we detail our computational methodology used to model CdS/MoS₂. In Sec. 3.1, we discuss electronic properties of the individual CdS surfaces and MoS₂ monolayer. In Sec. 3.2, we examine the interfacial charge transfer and band realignment that occurs in the heterojunction. In Sec. 3.3, we investigate the influence of sulfur vacancies on the CdS/MoS₂ interface. Finally, Sec. 4 summarizes our findings and discusses their implications for understanding the mechanisms behind the enhanced photocatalytic performance of CdS/MoS₂.

2 Computational Methods

In this section, we highlight the computational methodology used to model the CdS/MoS₂ heterojunction. Our structural model

of the heterojunction is composed of the wurtzite phase of CdS and monolayer 2H phase of MoS₂. To construct the interface, we first optimize the bulk lattice constants of both materials. The resulting values are consistent with previous first-principles and experimental studies as shown in Table S1^{33–36}.

Using these optimized lattice constants, we cleave the (100)- and (001)-CdS surfaces from the bulk crystal. Notably, the (001)-CdS surface contains 0.5 e[−] per unpassivated Cd bond, making it unstable³⁷. To satisfy the electron counting model³⁸, we introduce one Cd vacancy per 2×2 unit cell [c(2×2) reconstruction]. This reconstruction is experimentally observed in similar surfaces, such as (001)-ZnSe³⁹. First-principles studies further indicate that this reconstruction induces planarization around the surface Cd atoms, consistent with passivation through electron transfer³⁷. In contrast, the stoichiometric (100)-CdS surface is nonpolar, requiring no such modification.

Extended surface slabs are essential for capturing bulk interactions that are absent in monolayer models and are crucial for accurately predicting the geometry, energetics, and electronic features of the surface layer⁴⁰. To construct an accurate yet computationally efficient slab model, we vary the number of CdS atomic layers and monitor the convergence of the work function and surface energy. We find that with three atomic layers, the changes in work functions of the (100)- and (001)-CdS surfaces are below 10 meV and variations in the surface energies are less than 1 meV/Å². These values are consistent with previous first-principles and experimental studies, as summarized in Table S2^{41–44}.

After determining the slab model, we interface the two materials aiming to find a small lattice mismatch (Δ_m) while maintaining a reasonably sized supercell. To achieve this, we systematically explored different integer multiples of the primitive surface unit cells of each material to identify pairs of supercells that closely match in-plane lattice vectors. In this study, we use a 3×3 (100)-CdS supercell with a 4×4 MoS₂ supercell resulting in $\Delta_{mx} = 2.03\%$ and $\Delta_{my} = 8.74\%$. For (001)-CdS, we use a 4×4 supercell with a 5×5 MoS₂ supercell, which gives $\Delta_{mx} = \Delta_{my} = 4.55\%$. We note that CdS/MoS₂ heterostructures mainly grow in nanowire and nanoparticle morphologies, which maintain coherent interfaces when lattice mismatch values are less than 10%, consistent with the values in this study⁴⁵. Table S5 summarizes the strain experienced by MoS₂ and the associated changes in its band gap.

Sulfur vacancies are among the most common native defects in CdS/MoS₂ heterostructures, owing to their low formation energies and thermodynamic stability under typical experimental growth conditions, as reported for bulk MoS₂³⁵. To investigate their effects, we introduce sulfur vacancies on top of the MoS₂ monolayer facing the vacuum positioned above a Cd atom, above a S atom, and within a hollow site as highlighted in Fig. S3. To accommodate these distinct configurations in the (100)-CdS/MoS₂ system, the surface was extended in the *x*-direction, resulting in an 8×4 supercell for CdS and a 10×5 supercell for MoS₂.

First-principles electronic structure calculations based on density functional theory (DFT) were conducted using the QUANTUM ESPRESSO software package (version 7.3)⁴⁶. Calculations were performed using optimized norm-conserving Van-



derbilt pseudopotentials⁴⁷, the generalized gradient approximation for exchange correlation interactions, and Perdew-Burke-Ernzerhof (PBE) functional⁴⁸. The DFT-D3 method is used to account for van der Waals dispersion interactions⁴⁹. The heterostructures were placed in a vacuum of 25 Å along the z-axis and the atomic coordinates were relaxed with an energy cutoff of 70 Ry until the interatomic forces and energy were below 10^{-2} eV/Å and 10^{-4} Hartree, respectively. The Brillouin zone was sampled by $2 \times 2 \times 1$ and $4 \times 4 \times 1$ Monkhorst-Pack grids for geometry optimization and density of states, respectively. The calculation of formation energy of defects, heterostructure binding energy, dipole moment, work function, surface energy, and charge density difference are detailed in Sec. S0.1.

3 Results and Discussions

3.1 Isolated components of the CdS/MoS₂ heterostructure

In this section, we examine the electronic properties of the CdS surfaces and MoS₂ monolayer in isolation. Upon relaxation, we find that both the (100)- and (001)-CdS surfaces undergo extensive reconstruction as depicted in Fig. S1 and quantified in Tables S3 and S4. The initially planar (100)-CdS surface becomes corrugated due to the presence of dangling bonds in the top layer. In contrast, the (001)-CdS surface exhibits planarization around the surface Cd atoms, in which the corrugated (001)-CdS surface becomes flattened upon relaxation, consistent with the previously noted effect of passivation via electron transfer. Although not quantified, we observe that the pristine monolayer MoS₂ remains largely unreconstructed after relaxation, in agreement with prior first-principles calculations⁵⁰. As shown in Table S2, the (001)-CdS surface has a higher surface energy than the (100)-CdS surface (0.90 J/m² vs. 0.28 J/m²), which is consistent with previous first-principles studies on CdS surfaces⁴². Experimental observations further corroborate this, showing that CdS preferentially grows along the (001) direction—often forming nanorod-like morphologies, particularly at elevated temperatures^{27,51}. This anisotropic growth is attributed to the higher reactivity of the (001) surface, which, due to its greater surface energy and higher density of dangling bonds, promotes nucleation and heteroepitaxial growth⁵².

Next, we examine band edges of both CdS surfaces and monolayer MoS₂. According to the first three columns of the diagram in Fig. 1, we anticipate that both (001)- and (100)-CdS surfaces will form a Type-II heterojunction with MoS₂. The band alignment indicates that electrons transfer from MoS₂ to CdS and holes migrate from CdS to MoS₂. This spatial separation of charge carriers can suppress recombination and enhance photocatalytic efficiency. However, contrary to this expected behavior, electron accumulation on MoS₂ is actually preferred for hydrogen evolution. MoS₂ is known to be an excellent hydrogen evolution reaction (HER) catalyst due to its near-zero free energy of adsorption of hydrogen^{53–55}.

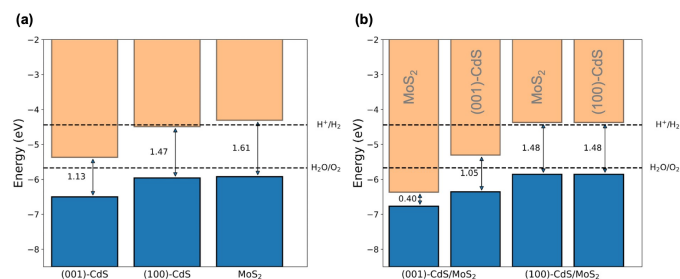


Fig. 1 Conduction (orange) and valence (blue) band edges for the (a) isolated components and (b) heterostructures with component contributions from MoS₂ (left) and CdS surface (right) are plotted with respect to vacuum. Corresponding band gap values (in eV) are given between the band edges. The redox potentials of water are indicated by the dotted lines.

3.2 Interfacial dipole formation and band alignment renormalization

In this section, we examine the interfacial charge transfer and band alignment renormalization that occur in the (001)- and (100)-CdS/MoS₂ heterojunctions. Upon relaxation, we obtain binding energies of -17.59 and -17.18 meV/Å² for (001)- and (100)-CdS/MoS₂, respectively. The negative values indicate that the formation of these heterostructures is both energetically favorable and spontaneous. Moreover, the magnitude of the binding energies fall within the typical range for van der Waals interactions (13–21 meV/Å²), suggesting that these forces dominate the interfacial adhesion⁵⁶. This interpretation is further supported by the relatively large interlayer distances of 3.12 and 3.04 Å for (001)- and (100)-CdS/MoS₂ (as shown in Fig. S2), which are significantly greater than the equilibrium Cd-S bond length of 2.55 Å, indicating the absence of covalent bonding across the interface. We also observe that (001)-CdS/MoS₂ has a more negative binding energy, which supports selective growth behavior noted earlier⁵².

Charge redistribution at the interface leads to the formation of interfacial dipole moments, as illustrated in Fig. 2. These dipole moments induce electron accumulation on MoS₂ and CdS for the (001)- and (100)-CdS/MoS₂ heterostructures, respectively. Notably, the interfacial dipole moment in (001)-CdS/MoS₂ (-2.51×10^{-6} Debye) is three orders of magnitude greater than that of (100)-CdS/MoS₂ (1.15×10^{-9} Debye). This difference may be explained by the polar nature of the (001)-CdS surface termination, which facilitates the transfer of electrons from CdS to the electron-deficient MoS₂ layer. This charge transfer arises from an interfacial dipole that points in the opposite direction, from MoS₂ toward CdS, compared to a nonpolar interface. In contrast, the (100)-CdS surface is nonpolar, which leads to a smaller dipole moment and weaker driving force for charge transfer. This can be further understood by comparing Figs. 1 and 2. In the (001)-CdS/MoS₂ case, the MoS₂ layer screens the large intrinsic dipole of (001)-CdS, becoming electron depleted in the process as highlighted in Fig. 2b where the charge density difference in



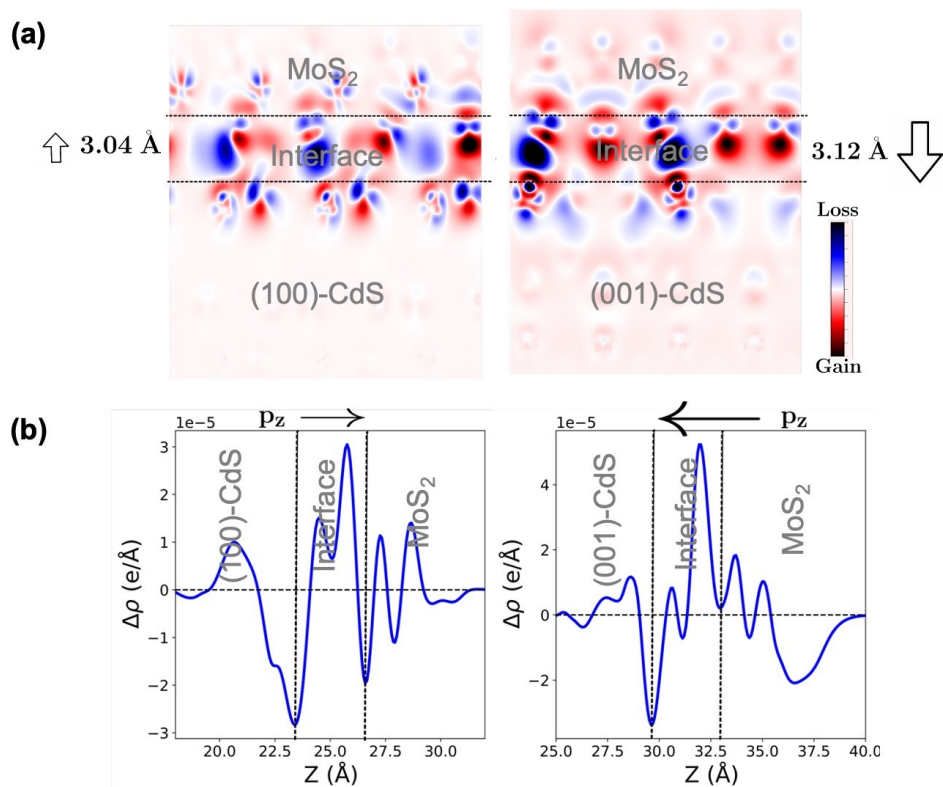


Fig. 2 (a) Charge density difference plot ($\Delta\rho = \rho_{\text{CdS/MoS}_2} - \rho_{\text{CdS}} - \rho_{\text{MoS}_2}$) and interlayer distances for the (001)-CdS/MoS₂ and (100)-CdS/MoS₂ systems. Red and blue regions indicate electron gain and loss, respectively. The dotted lines mark the position of the heterojunction interface. The arrows highlight the strength and direction of the interfacial dipole moment (\mathbf{p}_z). (b) Planar-averaged charge density difference profile averaged along the z-axis.

MoS₂ is largely negative. As a result, its bands shift downward to align more closely with those of (001)-CdS depicted clearly in Fig. 1b. Conversely, in the (100)-CdS/MoS₂ case, it is the CdS layer that screens the dipole, leaving the band edges of MoS₂ largely unchanged as shown by the relatively neutral charge density difference across the MoS₂ region in Fig. 2b. This modulation of band edges gives rise to a Type-III band alignment in (001)-CdS/MoS₂ in which the bands of MoS₂ are below that of CdS, and a homojunction-like alignment in (100)-CdS/MoS₂ in which the bandgaps of MoS₂ and CdS are nearly identical with minimal band offset as shown in Fig. 3. These assignments are further supported from density of states presented in Fig. S6. In the (001)-CdS/MoS₂ heterostructure, the band offset between the conduction band minimum of MoS₂ and the valence band maximum of CdS is relatively small, at around 30 meV. We note that this assignment is sensitive to variations in the strain of MoS₂, thermal fluctuations, and solvation effects, which are expected to further re-normalize the band edges and remain active topics of investigation. Nevertheless, these findings are in contrast with the Type-II band alignments predicted for both heterostructures based on isolated components in Fig. 1, highlighting the limitations of Anderson's rule in predicting band alignment⁵⁷. In particular, the ultrathin nature of the MoS₂ monolayer limits its ability to screen interfacial dipole moments, resulting in substantial band edge renormalization. Similar observations have been reported in other systems, such as BiFeO₃/MoS₂⁵⁸ and (0001)-

GaN/MoS₂⁵⁹, where interfacial dipole effects alter the expected alignment. These observations underscore the necessity of explicitly modeling the interface to capture the electrostatic and electronic interactions that govern the actual band alignment in heterostructures.

The Type-III alignment observed in (001)-CdS/MoS₂ facilitates charge separation, enabling electron transfer and accumulation on MoS₂. This is consistent with the time-dependent DFT (TDDFT) study by Cheng et al.²², who observed a two-stage increase in transferred electron density on MoS₂—an initial slow rise attributed to electron-phonon coupling, followed by a rapid 10% increase within 20 fs. They linked this acceleration to the formation of an interfacial dipole that shifts MoS₂ states downward relative to CdS, enabling direct electronic state intermixing. This electron transfer pathway is further corroborated by transient absorption (TA) spectroscopy measurements^{60,61}, which observe similar ultrafast carrier dynamics across the CdS/MoS₂ interface. Taken together, these theoretical and experimental findings reinforce our conclusion that the pronounced interfacial dipole in (001)-CdS/MoS₂ plays an important role in modulating band alignment and driving rapid interfacial electron transfer. Additionally, as highlighted in Figure S5, the band renormalization in (001)-CdS/MoS₂ results in band gap narrowing in both MoS₂ and CdS, which may enable the absorption of low-energy photons. However, the close proximity between the VBM of (001)-CdS and CBM of MoS₂ enables band-to-band tunneling, which



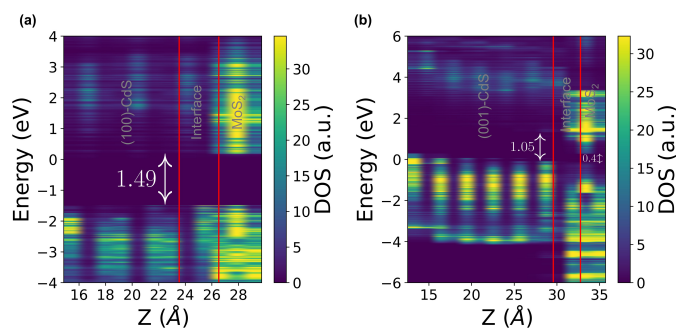


Fig. 3 Spatially resolved density of states (SRDOS) for the (a) (001)-CdS/MoS₂ and (b) (100)-CdS/MoS₂ systems. DOS intensity is mapped to a color for each energy level (with respect to Fermi level) and position along the z-axis of the heterostructure. The interfacial region is marked by the red lines. CdS and MoS₂ regions are marked accordingly along with corresponding band gaps.

can increase the likelihood of interfacial recombination⁶².

The homojunction-like band alignment, in the (100)-CdS/MoS₂ heterojunction provides little driving force for charge carrier separation. However, interfacing MoS₂ with the (100)-CdS surface results in a band gap increase of approximately 0.01 eV compared to the isolated (100)-CdS surface. In this configuration, the CBM is positioned above the H⁺/H₂ reduction potential and VBM below the H₂O/O₂ oxidation potential, as shown in Fig. 1. While the difference lies within the estimated 10 meV convergence threshold of the calculated band edges—determined from DOS sampling—the (100)-CdS/MoS₂ interface exhibits more favorable band alignment with the water redox potentials, suggesting enhanced suitability for photocatalytic hydrogen evolution⁶³. This band gap widening leads to a more favorable band edge alignment with the water redox potentials, in support that (100)-CdS/MoS₂ is a promising candidate for photocatalytic hydrogen evolution⁶³. These findings are further supported by the DFT study of Zhang et al., which reported that the (100)-CdS/MoS₂ heterojunction exhibits superior photocatalytic performance compared to (001)-CdS/MoS₂, attributed to its extended light absorption edge, faster charge carrier mobility, and enhanced visible light absorption²¹.

Based on these findings, we propose that the two CdS facets may act synergistically to enhance photocatalytic activity. The (001)-CdS facet promotes spatial separation of photogenerated charge carriers, while its band gap narrowing extends the light absorption range into the lower-energy region of the spectrum. In contrast, the (100)-CdS facet retains a larger band gap, enabling absorption of higher-energy photons and providing band edge positions well-aligned with the redox potentials required for water splitting reactions.

3.3 Sulfur vacancies in the CdS/MoS₂ heterostructure

In this section, we investigate the influence of sulfur vacancies on the CdS/MoS₂ heterostructure. Specifically, sulfur vacancies on top of the MoS₂ monolayer facing the vacuum positioned above

a Cd atom, above a S atom, and within a hollow site as highlighted in Fig. S3. For (001)-CdS/MoS₂, although the introduction of sulfur vacancies leads to an overall charge redistribution at the interface, the local charge environment around the vacancies remains relatively consistent across different defect positions as shown in Fig. 4a. This is reflected in the Bader charge difference (ΔQ) between the sulfur atoms directly beneath the vacancies before and after geometry optimization, which varies by no more than 0.006 *e*, indicating that the effect of the sulfur vacancy is uniformly distributed in this facet. By contrast, sulfur vacancies in (100)-CdS/MoS₂ produce qualitatively different charge density difference profiles, with the local ΔQ values varying by up to 0.055 *e*—nearly an order of magnitude greater than in the (001)-facet. To further quantify these observations, we present the planar-averaged charge density difference profiles in Fig. 4b. For all sulfur vacancy configurations in (001)-CdS/MoS₂, the interfacial dipole moments consistently point in the same direction, aiding in the electron accumulation on the CdS. Conversely, (100)-CdS/MoS₂ exhibits a more diverse charge redistribution behavior with respect to different locations of the sulfur vacancy, consistent with the qualitatively different two-dimensional profiles among the three sulfur vacancy locations. Specifically, only the sulfur vacancy above the Cd atom leads to a dipole moment that favors electron accumulation on CdS, while those on the S atom and hollow site promote electron accumulation on MoS₂—the desired outcome for facilitating charge separation. These findings highlight that charge redistribution and the associated energetics induced by sulfur vacancies are facet-dependent, with (100)-CdS/MoS₂ showing more sensitive, localized responses when compared to the (001) facet.

Next, we plot the band edges of the heterostructures containing sulfur vacancies to assess the impact of these defects on band alignment. In the (001)-CdS/MoS₂ system shown in Fig. S7a, the introduction of sulfur vacancies does not induce significant changes to the overall electronic structure. Notably, the Type-III band alignment observed in the pristine interface is preserved, with the CBM of MoS₂ remaining below the VBM of CdS. Sulfur vacancies cause a slight reduction in the band offset between these states to approximately 10 meV—about 20 meV lower than in the pristine system. This small change appears to be largely independent of the specific vacancy site, consistent with previously observed uniform charge redistribution trends. Although the reduction in band offset is minimal and comparable to thermal energy at room temperature, it could potentially enhance electronic coupling across the interface, which in turn may increase the likelihood of recombination. However, given the subtlety of this effect, detailed calculations of electronic coupling and recombination dynamics are necessary to fully assess its impact on photocatalytic performance. Similarly, sulfur vacancies in the (100)-CdS/MoS₂ system do not alter the homojunction-like alignment as shown in Fig. S6b. However, we observe that these vacancies introduce defect states 0.15 and 0.1 eV below the CBM for sulfur vacancies located on top of the Cd atom and S atom, respectively as highlighted in Fig. 5. The small energy separation between the defect states and the CBM may suggest that these are shallow in nature, with predominantly Mo *d*-orbital character as illustrated



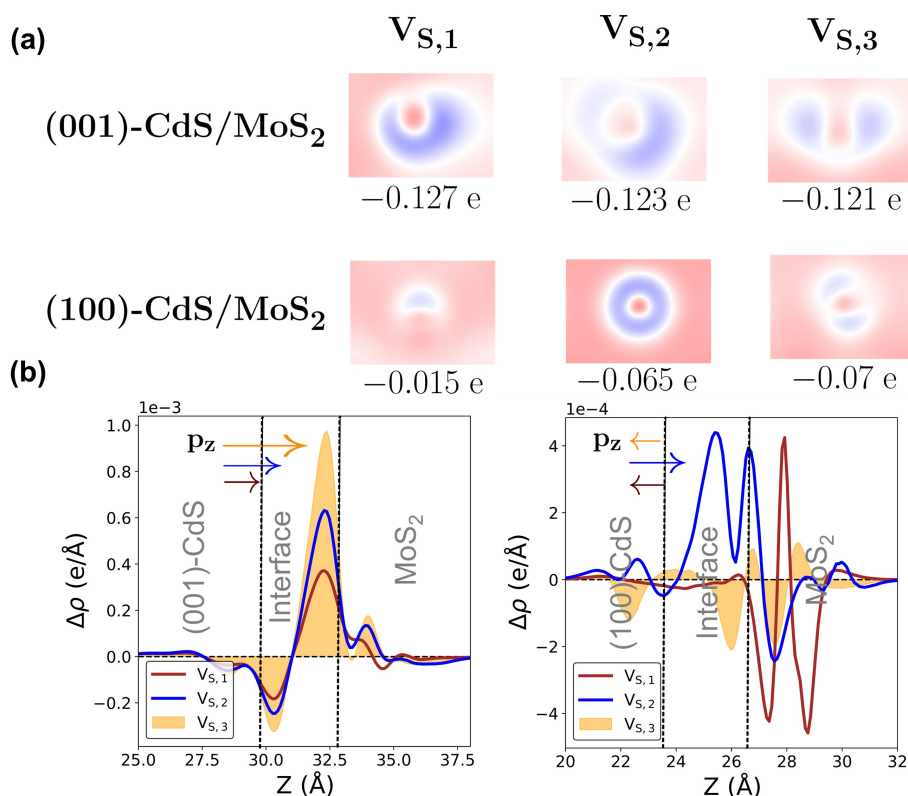


Fig. 4 (a) Local charge density difference ($\Delta\rho = \rho_{\text{CdS/MoS}_2} - \rho_{\text{CdS}} - \rho_{\text{MoS}_2}$) profiles viewed along the z -axis of sulfur atoms directly below various sulfur vacancies for the (001)- and (100)-CdS/MoS₂ heterostructures. Bader charge difference of these sulfur atoms before and after geometry optimization is given below the profiles in number of electrons. Red and blue regions indicate electron gain and loss, respectively. (b) Planar-averaged charge density difference profiles averaged along the z -axis. The CdS side, MoS₂ side, and interface of the heterojunction are marked. The colored arrows indicate the relative magnitudes and directions of interfacial dipole moments (\mathbf{p}_z) for the various defects. Sulfur vacancy position notation is given in Fig. S3.

in Fig. S7b.

These defects have several critical effects on photocatalytic performance. Since the associated defect levels lie below the CBM, they can extend the material's photoresponse by enabling sub-bandgap photon absorption, allowing the capture of longer-wavelength light²⁹. In addition, these shallow defect states can act as electron traps^{64,65}, temporarily localizing charge carriers and thereby suppressing rapid electron-hole recombination. When the energy levels of these traps are favorably aligned near the H⁺/H₂ reduction potential, they may also serve as active sites for facilitating the hydrogen evolution reaction (HER), particularly in systems like (100)-CdS/MoS₂. For example, sulfur vacancies in MoS₂ have been shown to activate its inert basal plane by tuning the free energy of adsorption of hydrogen adsorption free energy closer to null^{31,32}. Shallow defects induced by anion vacancies have been shown to enhance photocatalytic efficiency in other systems, such as g-C₃N₄/MoS₂⁶⁶, where trap states facilitated interfacial electron transfer, and TiO₂⁶⁷, where surface defects suppress charge recombination and broaden the spectral absorption range. We note, however, that a more conclusive identification of HER active sites would require a detailed analysis of water adsorption geometries and reaction pathways, including associated energy barriers.

Given the role of defects in facilitating directional interfacial

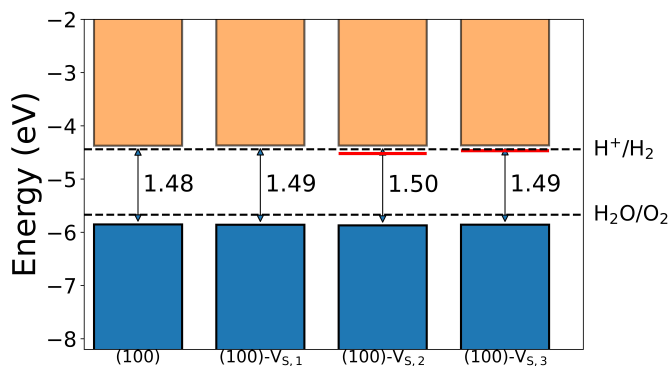


Fig. 5 Conduction (orange) and valence (blue) band edges plotted with respect to vacuum. Defect states are plotted in red. The second defect configuration, corresponding to a sulfur vacancy above a Cd atom, is most stable for (100)-CdS/MoS₂ (see Fig. 6). Notation used is (CdS surface interfaced with MoS₂)-defect number (see Fig. S3 for structures corresponding to defect numbering). Corresponding band gap values (in eV) are given between the band edges. The redox potentials of water are indicated by the dotted lines.



charge transfer and enhancing the HER on (100)-CdS/MoS₂, we explore the potential of defect engineering as a viable strategy to boost photocatalytic performance. To this end, we compute and compare the formation energies of various intrinsic defects, as shown in Fig. 6. Our results reveal that the sulfur vacancy above the Cd atom yields the most stable sulfur vacancy formation on both (100)- and (001)-CdS/MoS₂, with the former being consistently more favorable by ~ 1.5 eV across all configurations. This substantial energy difference suggests that sulfur vacancies are more likely to form at the MoS₂ layer when interfaced with the (100) facet of CdS compared to the (001) facet. This difference may be attributed to strain effects. As noted earlier, the (100)-CdS/MoS₂ heterostructure induces compressive strain in the MoS₂ monolayer, whereas (001)-CdS/MoS₂ induces tensile strain. Previous studies have shown that compressive strain lowers the sulfur vacancy formation energy in MoS₂, while tensile strain increases it^{68,69}. This trend is consistent with the lower vacancy formation energy observed for (100)-CdS/MoS₂. The energy differences among individual defect configurations for each of the two facets are relatively small (less than ~ 110 meV), making precise site-selective defect control difficult. Nevertheless, the pronounced contrast in defect energetics between the (100) and (001) facets has clear implications. In particular, higher concentrations of sulfur vacancies are expected on the (100)-CdS/MoS₂, which correspond to high concentrations of vacancies above S atoms and hollow sites that we find to promote the favorable charge separation. By contrast, while sulfur vacancies at the (001)-CdS/MoS₂ interface are expected to hinder the desired charge separation, they also occur at lower concentrations.

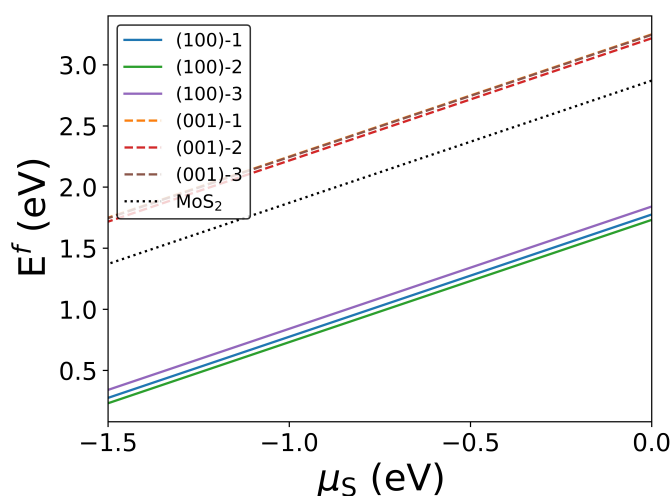


Fig. 6 Formation energies of sulfur vacancies on the CdS surface. The sulfur vacancy above the Cd atom is the most stable for both the (100)- and (001)-CdS/MoS₂ heterojunctions. Notation used is (CdS surface interfaced with MoS₂)-defect number. The formation energy of a sulfur vacancy on monolayer MoS₂ is given by the black dotted line. Sulfur vacancy position notation is given in Fig. S3.

4 Conclusion

In this study, we investigated the role of facet orientation and interfacial point defects on the photocatalytic performance of CdS/MoS₂ heterojunctions. First, we find that the van der Waals heterojunction formation is energetically favorable, inducing interfacial charge redistribution and dipole formation, with a greater magnitude observed for (001)-CdS/MoS₂. This leads to a downwards shift of MoS₂ band edges relative to (001)-CdS due to a combination of strain and screening interactions, while (100)-CdS/MoS₂ exhibits minimal band renormalization. The modulation of band edges results in a Type-III alignment for (001)-CdS/MoS₂ and homojunction-like alignment for (100)-CdS/MoS₂. These findings highlight the importance of explicitly modeling the interface to characterize band offsets. In particular, we find that the CBM of the (100)-CdS/MoS₂ heterostructure lies above the H⁺/H₂ reduction potential and VBM lies below the H₂O/O₂ oxidation potential, which makes it an ideal photocatalyst system for water-splitting reactions.

Based on these findings, we propose that the enhanced photocatalytic activity observed in CdS/MoS₂ arises from a synergistic effect between the two CdS facets. The (001)-CdS facet facilitates spatial separation of photogenerated charge carriers, and its band gap narrowing extends light absorption into lower-energy regions of the spectrum. In contrast, the (100)-CdS facet maintains a wider band gap, allowing absorption of higher-energy photons and offering band edge positions that are well-aligned with the redox potentials necessary for water splitting.

Next, we examined the effect of sulfur vacancies on photocatalytic activity. In (001)-CdS/MoS₂, all vacancy sites exhibited similar charge density difference profiles, characterized by interfacial dipoles that promote electron accumulation on the CdS side. Correspondingly, the introduction of sulfur vacancies does not significantly alter the overall electronic structure, and the system retains its Type-III band alignment. In contrast, (100)-CdS/MoS₂ shows more varied responses to sulfur vacancies. Vacancies located above the S atom of MoS₂ and at hollow sites lead to charge redistribution patterns that favor electron accumulation on MoS₂—an effect that may enhance interfacial charge transfer toward active sites. Furthermore, sulfur vacancies positioned directly above Cd and S atoms introduce shallow defect states approximately 0.1 and 0.15 eV below the CBM, respectively. These defect levels are energetically aligned with the H⁺/H₂ reduction potential, indicating their potential role in facilitating the hydrogen evolution reactions. Although the energy differences between individual defect configurations within each facet are relatively small, sulfur vacancies can enhance the interfacial dipole moment on (001) surfaces and active sites on (100) surfaces. This presents a practical strategy for tuning photocatalytic activity in CdS/MoS₂ heterostructures through controlled exposure and defect incorporation.

There are several future directions for elucidating ambiguities observed in CdS/MoS₂ band alignment measurements. Experimentally, Mott-Schottky analysis is commonly used to extract the flat-band potentials of CdS and MoS₂ separately, then used to infer band alignment in the heterostructure. However, this



method is highly sensitive to measurement conditions such as electrolyte pH⁷⁰ and relies on assumptions like the depletion approximation⁷¹, which may not be valid for monolayer MoS₂. More critically, it neglects interfacial effects such as charge redistribution, which we show play a significant role in re-normalizing the band alignment. Additionally, most CdS/MoS₂ heterostructures reported in literature are synthesized as nanoparticles rather than atomically precise interfaces, leading to disordered junctions and considerable interfacial strain. This is particularly important for monolayer MoS₂, which exhibits a high deformation potential and is known to be highly sensitive to strain—strongly affecting its band edge positions and, by extension, the overall band alignment⁷². From a theoretical standpoint, thermal effects such as lattice expansion and phonon-induced atomic vibrations, and solvent-induced polarization can shift semiconductor energy levels from few meV⁷³ to several hundred meV⁷⁴. Accurate modeling of band offsets therefore requires accounting for both thermal and solvation effects as demonstrated in other systems⁷⁵.

Overall, our findings offer a pathway for rational design of facet- and defect-engineered CdS/MoS₂ heterostructures with enhanced photocatalytic performance. The identification of facet-selective defect effects and formation energies provides a strategy to selectively stabilize beneficial defects—such as shallow states aligned with the HER potential—while minimizing recombination pathways. More broadly, this work highlights the importance of atomically resolved models in understanding and optimizing complex semiconductor heterojunctions, and it lays the foundation for future experimental and theoretical efforts to control interfacial energetics in photocatalytic systems.

5 Author contributions

B.K.: Formal analysis; Writing - original draft; Writing - review & editing. R.A.: Conceptualization; Supervision; Writing - review & editing. W.W.: Conceptualization; Funding acquisition; Project administration; Supervision; Writing - review & editing.

6 Conflicts of interest

There are no conflicts to declare.

7 Data availability

The dataset (~3.5 GB) generated and analyzed in the current study is openly available in Zenodo (URL: <https://doi.org/10.5281/zenodo.15712114>). The dataset contains input files, relaxed structure files, charge density difference plots, partially- and spatially-resolved density of states, data related to defect formation energy; each data type is accompanied with an electronic notebook.

8 Acknowledgments

This work is supported by a grant from The Welch Foundation (Grant No. F-2172-20230405). The authors acknowledge the Texas Advanced Computing Center (TACC) at The University of Texas at Austin (URL: <http://www.tacc.utexas.edu>) for HPC resources.

References

- 1 T. Yusaf, M. Laimon, W. Alrefae, K. Kadirgama, H. A. Dhahad, D. Ramasamy, M. K. Kamarulzaman and B. Yousif, *Applied Sci-*

ences, 2022, **12**, 781.

- 2 M. Jaradat, O. Alsotary, A. Juaidi, A. Albatayneh, A. Alzoubi and S. Gorjian, *Energies*, 2022, **15**, 9039.
- 3 M. Ji and J. Wang, *International Journal of Hydrogen Energy*, 2021, **46**, 38612–38635.
- 4 S. J. Peighambardoust, S. Rowshanzamir and M. Amjadi, *International journal of hydrogen energy*, 2010, **35**, 9349–9384.
- 5 C. Acar and I. Dincer, *Journal of cleaner production*, 2019, **218**, 835–849.
- 6 K. Schmietendorf, J. Peinke and O. Kamps, *The European Physical Journal B*, 2017, **90**, 1–6.
- 7 P. Zhou, I. A. Navid, Y. Ma, Y. Xiao, P. Wang, Z. Ye, B. Zhou, K. Sun and Z. Mi, *Nature*, 2023, **613**, 66–70.
- 8 A. Mills and S. Le Hunte, *Journal of photochemistry and photobiology A: Chemistry*, 1997, **108**, 1–35.
- 9 A. Pan and X. Zhu, *Semiconductor Nanowires*, Elsevier, 2015, pp. 327–363.
- 10 H. Matsumoto, T. Sakata, H. Mori and H. Yoneyama, *The Journal of Physical Chemistry*, 1996, **100**, 13781–13785.
- 11 L. Wei, Z. Guo and X. Jia, *Catalysis Letters*, 2021, **151**, 56–66.
- 12 D. Fermín, E. Ponomarev and L. Peter, *Journal of Electroanalytical Chemistry*, 1999, **473**, 192–203.
- 13 J. Low, J. Yu, M. Jaroniec, S. Wageh and A. A. Al-Ghamdi, *Advanced materials*, 2017, **29**, 1601694.
- 14 X. Zong, H. Yan, G. Wu, G. Ma, F. Wen, L. Wang and C. Li, *Journal of the American Chemical Society*, 2008, **130**, 7176–7177.
- 15 T. F. Jaramillo, K. P. Jørgensen, J. Bonde, J. H. Nielsen, S. Hørch and I. Chorkendorff, *science*, 2007, **317**, 100–102.
- 16 Y. Liu, Y.-X. Yu and W.-D. Zhang, *The Journal of Physical Chemistry C*, 2013, **117**, 12949–12957.
- 17 Y. Min, G. He, Q. Xu and Y. Chen, *Journal of Materials Chemistry A*, 2014, **2**, 2578–2584.
- 18 F. Ma, Y. Wu, Y. Shao, Y. Zhong, J. Lv and X. Hao, *Nano Energy*, 2016, **27**, 466–474.
- 19 Y. Zhong, G. Zhao, F. Ma, Y. Wu and X. Hao, *Applied Catalysis B: Environmental*, 2016, **199**, 466–472.
- 20 X. Lian, M. Niu, Y. Huang and D. Cheng, *Journal of Physics and Chemistry of Solids*, 2018, **120**, 52–56.
- 21 J.-R. Zhang, Y.-Q. Zhao, L. Chen, S.-F. Yin and M.-Q. Cai, *Applied Surface Science*, 2019, **469**, 27–33.
- 22 K. Cheng, H. Wang, J. Bang, D. West, J. Zhao and S. Zhang, *The Journal of Physical Chemistry Letters*, 2020, **11**, 6544–6550.
- 23 K. Chang, M. Li, T. Wang, S. Ouyang, P. Li, L. Liu and J. Ye, *Advanced Energy Materials*, 2015, **5**, 1402279.
- 24 L. Lin, S. Huang, Y. Zhu, B. Du, Z. Zhang, C. Chen, X. Wang and N. Zhang, *Dalton Transactions*, 2019, **48**, 2715–2721.
- 25 G. He, Y. Zhang and Q. He, *Catalysts*, 2019, **9**, 379.
- 26 K. Hamid, M. Z. B. Mukhlis and M. T. Uddin, *RSC advances*, 2024, **14**, 38908–38923.
- 27 W. Zheng, W. Feng, X. Zhang, X. Chen, G. Liu, Y. Qiu,



- T. Hasan, P. Tan and P. A. Hu, *Advanced Functional Materials*, 2016, **26**, 2648–2654.
- 28 X. Liu, J. Li and W. Yao, *ACS omega*, 2020, **5**, 27463–27469.
- 29 H. Yu, L. Qu, M. Zhang, Y. Wang, C. Lou, Y. Xu, M. Cui, Z. Shao, X. Liu, P. Hu *et al.*, *Advanced Optical Materials*, 2023, **11**, 2202341.
- 30 S. Bai, N. Zhang, C. Gao and Y. Xiong, *Nano Energy*, 2018, **53**, 296–336.
- 31 C. Tsai, H. Li, S. Park, J. Park, H. S. Han, J. K. Nørskov, X. Zheng and F. Abild-Pedersen, *Nature communications*, 2017, **8**, 15113.
- 32 H. Li, C. Tsai, A. L. Koh, L. Cai, A. W. Contryman, A. H. Fraga-pane, J. Zhao, H. S. Han, H. C. Manoharan, F. Abild-Pedersen *et al.*, *Nature materials*, 2016, **15**, 48–53.
- 33 T. G. Edossa and M. M. Woldemariam, *Advances in Condensed Matter Physics*, 2020, **2020**, 4693654.
- 34 S.-H. Wei and S. Zhang, *Physical review B*, 2000, **62**, 6944.
- 35 H.-P. Komsa and A. V. Krashenninnikov, *Physical Review B*, 2015, **91**, 125304.
- 36 T. Böker, R. Severin, A. Müller, C. Janowitz, R. Manzke, D. Voß, P. Krüger, A. Mazur and J. Pollmann, *Physical Review B: Condensed Matter and Materials Physics*, 2001, **64**, year.
- 37 J. Y. Rempel, B. L. Trout, M. G. Bawendi and K. F. Jensen, *The Journal of Physical Chemistry B*, 2005, **109**, 19320–19328.
- 38 M. Pashley, *Physical Review B*, 1989, **40**, 10481.
- 39 H. Cornelissen, D. Cammack and R. Dalby, *Journal of Vacuum Science & Technology B: Microelectronics Processing and Phenomena*, 1988, **6**, 769–772.
- 40 A. Kokalj and M. Causà, *Journal of Physics: Condensed Matter*, 1999, **11**, 7463.
- 41 Y. Ma, Y. Dai, W. Wei, X. Liu and B. Huang, *Journal of Solid State Chemistry*, 2011, **184**, 747–752.
- 42 A. S. Barnard and H. Xu, *The Journal of Physical Chemistry C*, 2007, **111**, 18112–18117.
- 43 K. Sasaki, *Japanese Journal of Applied Physics*, 1974, **13**, 933.
- 44 R. Minibaev, A. Bagatur'yants and D. Bazhanov, *Nanotechnologies in Russia*, 2010, **5**, 191–197.
- 45 K. L. Kavanagh, *Semiconductor Science and Technology*, 2010, **25**, 024006.
- 46 P. Giannozzi, S. Baroni, N. Bonini, M. Calandra, R. Car, C. Cavazzoni, D. Ceresoli, G. L. Chiarotti, M. Cococcioni, I. Dabo *et al.*, *Journal of physics: Condensed matter*, 2009, **21**, 395502.
- 47 D. Hamann, *Physical Review B—Condensed Matter and Materials Physics*, 2013, **88**, 085117.
- 48 J. P. Perdew, K. Burke and M. Ernzerhof, *Physical review letters*, 1996, **77**, 3865.
- 49 S. Grimme, J. Antony, S. Ehrlich and H. Krieg, *The Journal of chemical physics*, 2010, **132**, year.
- 50 K. Santosh, R. C. Longo, R. Addou, R. M. Wallace and K. Cho, *Nanotechnology*, 2014, **25**, 375703.
- 51 Y. Li, X. Li, C. Yang and Y. Li, *Journal of Materials Chemistry*, 2003, **13**, 2641–2648.
- 52 S.-M. Ko, J.-H. Kim, Y.-H. Ko, Y. H. Chang, Y.-H. Kim, J. Yoon, J. Y. Lee and Y.-H. Cho, *Crystal growth & design*, 2012, **12**, 3838–3844.
- 53 J. Xie, H. Zhang, S. Li, R. Wang, X. Sun, M. Zhou, J. Zhou, X. W. Lou and Y. Xie, *Advanced materials*, 2013, **25**, 5807–5813.
- 54 B. Hinnemann, P. G. Moses, J. Bonde, K. P. Jørgensen, J. H. Nielsen, S. Hørch, I. Chorkendorff and J. K. Nørskov, *Journal of the American Chemical Society*, 2005, **127**, 5308–5309.
- 55 G. Li, D. Zhang, Q. Qiao, Y. Yu, D. Peterson, A. Zafar, R. Kumar, S. Curtarolo, F. Hunte, S. Shannon *et al.*, *Journal of the American Chemical Society*, 2016, **138**, 16632–16638.
- 56 T. Björkman, A. Gulans, A. V. Krashenninnikov and R. M. Nieminen, *Physical review letters*, 2012, **108**, 235502.
- 57 R. L. Anderson, *Solid-State Electronics*, 1962, **5**, 341–351.
- 58 J.-Q. Dai, X.-W. Wang and T.-F. Cao, *The Journal of Physical Chemistry C*, 2019, **123**, 3039–3047.
- 59 H. Henck, Z. Ben Aziza, O. Zill, D. Pierucci, C. H. Naylor, M. G. Silly, N. Gogneau, F. Oehler, S. Collin, J. Brault *et al.*, *Physical Review B*, 2017, **96**, 115312.
- 60 S. Zhang, S. Li, M. Zhou, X. Li, Y. Wang, S. Suo, C. Chen, Z. Zhang, R. Zhang, B. Jin *et al.*, *Separation and Purification Technology*, 2025, **355**, 129664.
- 61 F. Zhang, Y. Hong, Z. Yao, Y. Li, S. Zheng, S. Yu, A. Yartsev, K. Zheng, T. Pullerits and Y. Zhou, *ACS Applied Nano Materials*, 2025.
- 62 C. Gong, H. Zhang, W. Wang, L. Colombo, R. M. Wallace and K. Cho, *Applied Physics Letters*, 2013, **103**, year.
- 63 M. C. Toroker, D. K. Kanan, N. Alidoust, L. Y. Isseroff, P. Liao and E. A. Carter, *Physical Chemistry Chemical Physics*, 2011, **13**, 16644–16654.
- 64 H. F. Haneef, A. M. Zeidell and O. D. Jurchescu, *Journal of Materials Chemistry C*, 2020, **8**, 759–787.
- 65 K. W. Böer and U. W. Pohl, *Semiconductor physics*, Springer Nature, 2023.
- 66 J. Xue, M. Fujitsuka and T. Majima, *ACS Applied Materials & Interfaces*, 2019, **11**, 40860–40867.
- 67 G. Dong, X. Wang, Z. Chen and Z. Lu, *Photochemistry and Photobiology*, 2018, **94**, 472–483.
- 68 R. Anvari and W. Wang, *Journal of Applied Physics*, 2024, **135**, year.
- 69 R. Albaridy, D. Periyangounder, D. Naphade, C.-J. Lee, M. Hedhili, Y. Wan, W.-H. Chang, T. D. Anthopoulos, V. Tung, A. Aljarb *et al.*, *ACS Materials Letters*, 2023, **5**, 2584–2593.
- 70 S. F. Lee, E. Jimenez-Relinque, I. Martinez and M. Castellote, *Catalysts*, 2023, **13**, 1000.
- 71 T. Kirchartz, W. Gong, S. A. Hawks, T. Agostinelli, R. C. MacKenzie, Y. Yang and J. Nelson, *The Journal of Physical Chemistry C*, 2012, **116**, 7672–7680.
- 72 H. Peelaers and C. G. Van de Walle, *Physical Review B—Condensed Matter and Materials Physics*, 2012, **86**, 241401.
- 73 Y. Zhang, Z. Wang, J. Xi and J. Yang, *Journal of Physics: Condensed Matter*, 2020, **32**, 475503.
- 74 Y. Ping, R. Sundararaman and W. A. Goddard III, *Physical*



chemistry chemical physics, 2015, **17**, 30499–30509.

- 75 G. Melani, W. Wang, F. Gygi, K.-S. Choi and G. Galli, *ACS Energy Letters*, 2024, **9**, 5166–5171.

- 76 A. Ferreira and L. Lobo, *The Journal of Chemical Thermodynamics*, 2011, **43**, 95–104.



Title:

Interfacial Electronic Structure Modulation by Facet Orientation and Sulfur Vacancies in CdS/MoS₂ Heterojunctions

Authors:

Beniam Kumela, Roozbeh Anvari, and Wennie Wang
McKetta Department of Chemical Engineering
The University of Texas at Austin

Data Availability Statement:

The dataset (~3.5 GB) generated and analyzed in the current study is openly available in Zenodo (URL:<https://doi.org/10.5281/zenodo.15712114>). The dataset contains input files, relaxed structure files, charge density difference plots, partially- and spatially-resolved density of states, data related to defect formation energy; each data type is accompanied with an electronic notebook.

